

3D Printed Intelligently Graded Functional Stiffness Foam for Sturdier Multi Stiffness Materials

B. A. Emery^{1,3}, D. Revier^{1,2}, V. Sarkar², M. Nakura², and J. I. Lipton^{1,2,3}

¹Mechanical Engineering, University of Washington, Stevens Way, Box 352600, Seattle, 98195, WA, USA.

²Computer Science and Engineering, University of Washington, 185 E Stevens Way NE, Seattle, 98195, WA, USA.

³Department of Mechanical & Industrial Engineering, Northeastern University, 334 Snell Engineering Center 360 Huntington Avenue, Boston, 02115, MA, USA.

Abstract

Foams are ubiquitous, being used in applications such as padding, insulation, and noise isolation. Bonding different density foams together produces undesired stress concentrations and boundary effects. Creating controlled gradients in foam properties has been a challenge for traditional and AM processes. Here we show how to use a form of material extrusion called Viscous Thread APrinting (VTP) to produce foams with multiple stiffnesses and continuous gradients between different stiffnesses. We do so by varying the path speed during extrusion to control the production of microstructures. We compare the process of producing discrete components and those with gradients, showing that those with gradients have higher strength in plane during tension, have no discontinuities in out of plane stiffness, and are less prone to forming cracks at the boundaries. We demonstrate the process in thermoplastic polyurethane (TPU).

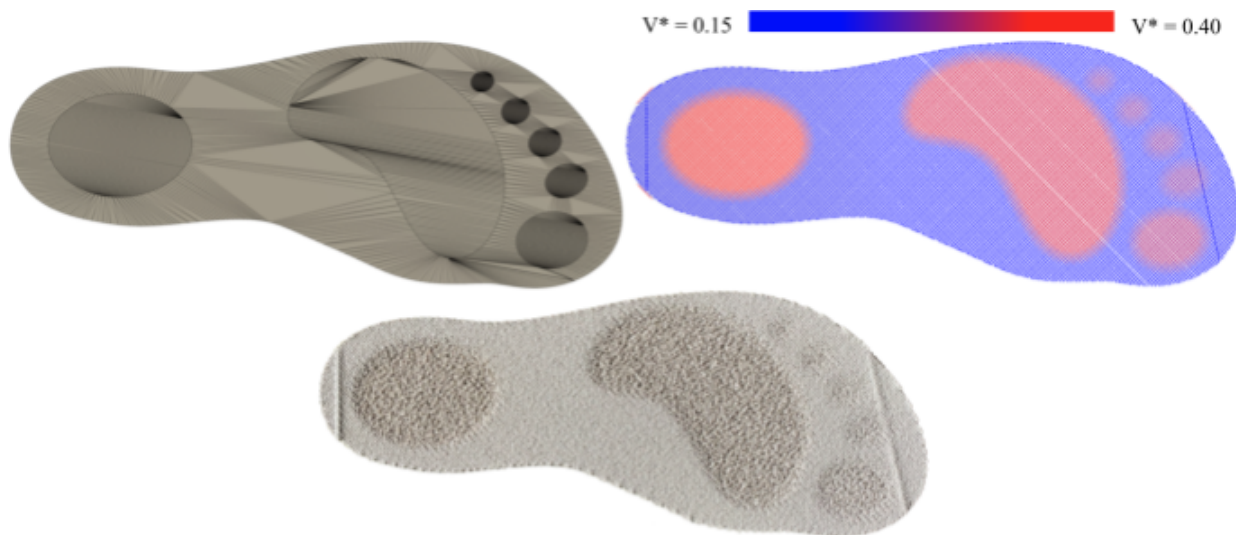


Figure 1. From top left to bottom center: Segmented STL, generated toolpath with V^* heatmap (and color scale), unmodified printed result.

Introduction

The field of additive manufacturing (AM), often referred to as "3D printing", has seen broad adoption across various applications, ranging from bioprinting for medical purposes to mechanical applications optimizing static and dynamic properties [1–6]. One of the unique features of 3D printing is the ability to program spatially variant mechanical properties by varying the underlying microstructure of an object. This is often used for things like acoustic cloaking, elastic cloaking, etc [7–9]. The microstructure is traditionally fabricated through two primary methods: 1) the explicit definition of the geometry or 2) implicit definition through tool path algorithms, such as volume-filling infills. In traditional manufacturing spatially varying properties is achieved through discrete lamination of materials of differing material properties. Our work pioneers the use of Viscous Thread Printing (VTP) to produce continuously graded materials within individual layers without the use of explicit cell design or intricate pathing algorithms. VTP uses the dynamics of the printing process to control the microstructure of the object and thus the underlying mechanical properties as a function of space.

Previous work on spatially variant mechanical material properties spans the use of topology optimization and expert design of cellular geometry. For explicit cell geometry, the printer's resolution must supersede the cellular structure's unit cell, typically by an order of magnitude or more [6,10–12]. These geometries necessitate intricate cellular design through structures like octet truss unit cells or topology optimization [13,14]. Yet, the cell size and design constraints often limit the applicability of explicitly defined cellular geometries in printed materials. For example, if a cell, such as an octet, is used, the unit cell must be constrained to a constant size in order to have a constant lattice spacing. This leaves the only control variable to be the diameter of the octet's trusses. Alternatively, in topology optimization the geometry is less constrained, but the design space is significantly larger and the problem quickly becomes intractable for large objects with a high degree of variation.

Our previous work with VTP created homogenous cellular structures with thermoplastic polyurethane (TPU) on standard Fused Filament Fabrication (FFF) printers. Through VTP, we generated foam structures at resolutions like the printer's native resolution by leveraging viscous thread instability (VTI), a phenomenon well-observed in 1D and 2D [15–18]. This principle, commonly exemplified by the pattern formed when honey is poured onto toast, enabled the creation of 3D structures when stacked. In the previous work we were able to control macroscopic material properties via VTP slicer input parameters and demonstrated the ability to control effective Young's modulus of the structure [19].

Building on that groundwork, this paper extends the utility of VTP to produce foams with multiple stiffnesses and continuous gradients between them [1,19]. By dynamically manipulating print parameters during slicing, we present an innovative method of generating graded foam structures on a standard FFF 3D printer. With this approach, we produce foams of varying stiffness along the principal axes, decreased print artifacts and boundary defects. In turn, these structures have improved failure performance over previous state-of-the-art by having higher fracture stress, fracture strain, and toughness. This showcases the potential of VTP to revolutionize the fabrication of graded foams for a multitude of applications [20].

Slicer

The key parameters to determine the coiling behavior of VTP are the dimensionless velocity variable V^* and the dimensionless height variable H^* ,

$$[1] \quad V^* = \frac{F}{C}$$

$$[2] \quad H^* = \frac{H}{\alpha D}$$

where F is the translation speed of the printhead, C is the exit speed of the material from the nozzle, H is the print height, D is the nozzle diameter and α is die swell, which is a material and process dependent constant that is determined empirically. Each of these variables can be controlled either explicitly or implicitly directly through G-code commands. Together, the V^*/H^* combination determines the type of coiling behavior exhibited and spatial frequency of the coiling as well as the coil diameter respectively.

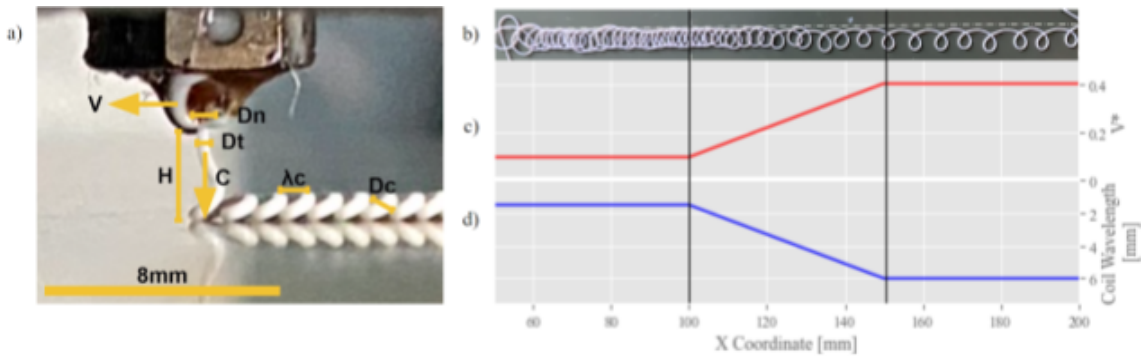


Figure. 2 a) Nozzle and thread as seen during VTP with annotations. b) VTP line demonstrating the resulting coiling due to dynamically changing V^* during a single linear travel move. c) V^* vs Travel plot horizontally to scale with b) and d). d) Coil Wavelength vs Travel plot horizontally to scale with b) and c).

There are three main regimes of coiling that are of interest for VTP foams: translating coiling, alternating coiling, and accumulation shown in Figure 3. Translating coiling results from a specific combination of V^*/H^* to produce a continuous path of overlapping loops of material. Translating coiling is interesting because it allows for the greatest number of interconnections of a single thread producing a structure that is dense while maintaining porosity and uniformity. Alternating coiling results in coils that are further spaced apart, producing fewer interconnections and a less dense structure. Finally, accumulation is the closest to traditional 3D printing techniques with a low V^* and low H^* and can produce parts that are nearly 100% dense and extrusion widths many times greater than the nozzle diameter via over-extrusion; however, it does not result in porous structures.

Controlling the V^*/H^* of a printed object is done implicitly by setting the correct print and extrusion speeds of the printing process. A G-code command G1 instructs the printer to move from its current position (x_0, y_0, z_0) to a new position (x, y, z) at a certain speed f , while extruding Δe length of material. In a G-code file this looks like **G1 Xx Yy Zz EΔe Ff**, where **G1** and the bold capital letters are alphabetical characters, and the lowercase letters represent numerical positions for the printer to parse. The x and y positions are determined by the object's infill toolpath, whereas z , Δe and f and values to be solved for.

The equations to generate G-code information from V^*/H^* inputs are then

$$[3] \quad z = \alpha D_N H^*$$

$$[4] \quad \Delta e = \frac{L A_T}{V A_F}$$

$$[5] \quad f = V^* \dot{E} \frac{A_F}{A_T}$$

where \dot{E} is the constant speed to feed filament into the nozzle, L is the Euclidean distance of the G-code move, and A_F and A_T are the filament and extruded thread areas respectively.

To generate spatially varying V^*/H^* we must first define areas of constant V^*/H^* and regions between them are called the transition regions. For notation we employ a subscript/superscript distinction, where the superscript will always denote a mesh-wise quantity, while a subscript will always denote a point-wise quantity.

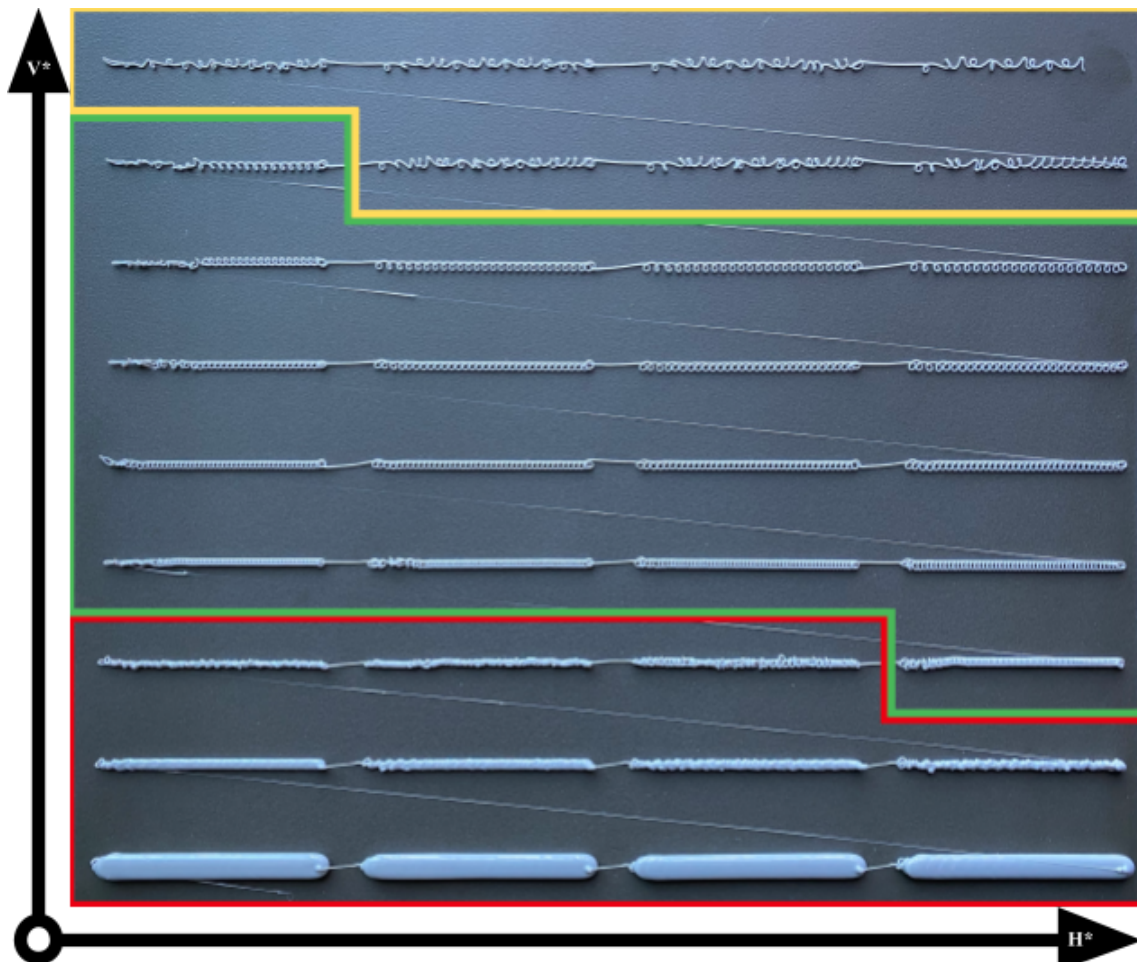


Figure 3. Example of a VTP spread demonstrating the effects of increasing H^* (along X-axis) and V^* (along Y-axis) as well as the three most significant coiling patterns for VTP. From top to bottom: alternating coiling (yellow border), translating coiling (green border), and accumulation (red border).

First, we load multiple submeshes into our custom slicer where Ω^j represents submesh j , $\partial\Omega^j$ represents the surface of Ω^j , and $\bar{\Omega} = \bigcup_{j \in M} \Omega^j$ is the total unioned mesh for the set of meshes M . These meshes are assumed to have constant cross-section in z and be non-overlapping but have some interfacing boundary. Each submesh is given a V^*/H^* pair assigned by the user, which we combine in the notation $\pi^j = \{(V^*)^j, (H^*)^j\}$. Other global variables, such as toolpath spacing, effective layer height, transition length and toolpath discretization length, and die swell are also set by the user up front.

We begin the slicing process by taking $\bar{\Omega}$ and feeding it to a traditional slicer (Slic3r) [21], which generates a toolpath traversing the entire space $\bar{\Omega}$. We then refine each of the linear toolpath sections into subsection of length $d \leq d_{max}$ which establishes the resolution of the V^*/H^* transitions.

Our transition algorithm associates each point along the toolpath p_i with interpolated π_i values by determining the weighted average of all the relevant submesh values. Relevant submeshes are determined by finding the distance between point p_i to $\partial\Omega^j$. Here we use the signed distance between p_i and $\partial\Omega^j$, where $D_i^j = SDF(p_i, \partial\Omega^j)$ and $D_i^j < 0 \Rightarrow p_i \in \Omega^j$. A point is said to be in a transition region Ω^T if the distance from point p_i to some $\partial\Omega^j$ is less than the user defined transition length, that is $|D_i^j| \leq D_T \Rightarrow p_i \in \Omega^T$. Then the weights contributed by each submesh are:

$$[6] \quad w_i^j = \begin{cases} 0 & p_i \notin \Omega^T, p_i \notin \Omega^j \\ \frac{1}{2} - \frac{D_i^j}{D_T} & p_i \in \Omega^T \\ 1 & p_i \notin \Omega^T, p_i \in \Omega^j \end{cases}$$

and the V^*/H^* values at point p_i are

$$[7] \quad \pi_i = \frac{\sum_{j \in M} w_i^j \cdot \pi^j}{\sum_{j \in M} w_i^j}$$

Mechanical Testing Methods

To test our slicer algorithm we compared samples made using our algorithm using various transition lengths, with the base materials and a simple base slicer. For all specimens labeled *TLXX* we implement the above method for a bisected ASTM dogbone structure. For specimens labeled *V0.15* and *V0.40* we slice those with a normal slicer and alter the output G-code file directly using equations 3-5 through a custom python script. Finally, for the specimen labeled *Zippered* we slice each half of the dogbone separately and then “zip” the two separate G-code files together where layer 1 of the first file is printed and then layer 1 of the second file is printed in sequence, and so on. This represents the previous state-of-the-art for multi-material printing of VTP foams [1].

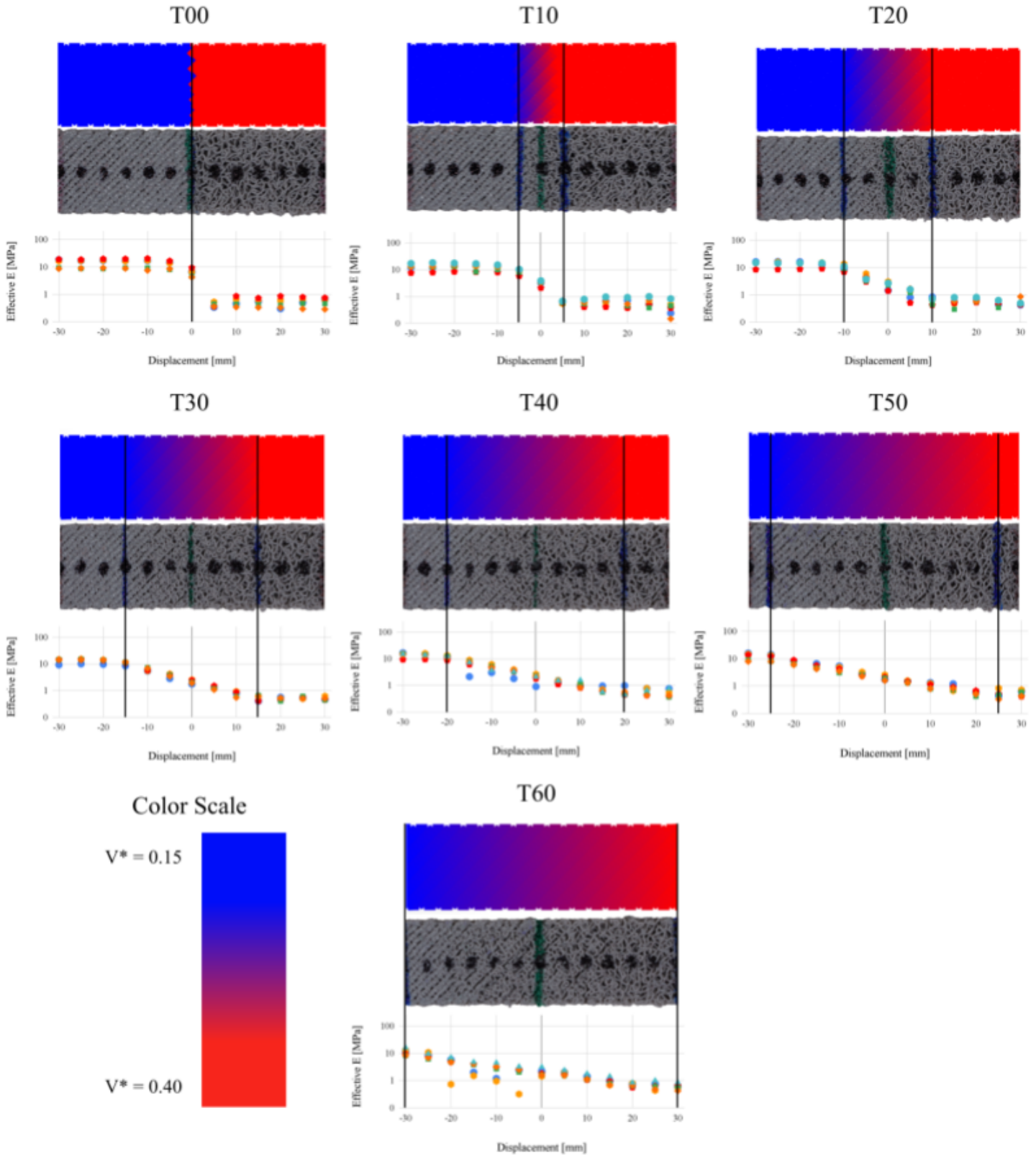


Figure 4. Each sample set's respective V^* heatmap (with color scale), printed transition region, and full effective Young's modulus data set. Each set of images is horizontally scaled as to facilitate vertical alignment for direct comparison of V^* , printed region, and effective modulus.

For our validation we printed ASTM Standard D638-10 Type III dogbones out of NinjaTek NinjaFlex TPU [22]. The dogbone STL was split in half at the midway mark and various transition lengths were applied to create a linear gradient in V^* along the axial direction of the dogbone. We conducted localized compression tests at 5 mm increments with a 10 mm diameter probe along the transition length to capture the variation in compressive modulus of the foams. The probe was printed on a Carbon M1 out of UMA-90 [23]. We then conducted ASTM Standard D638-10 tensile tests on an Instron 68SC-2 to measure the effective tensile modulus of the dogbone specimen as well capture fracture stress, fracture strain, and toughness.

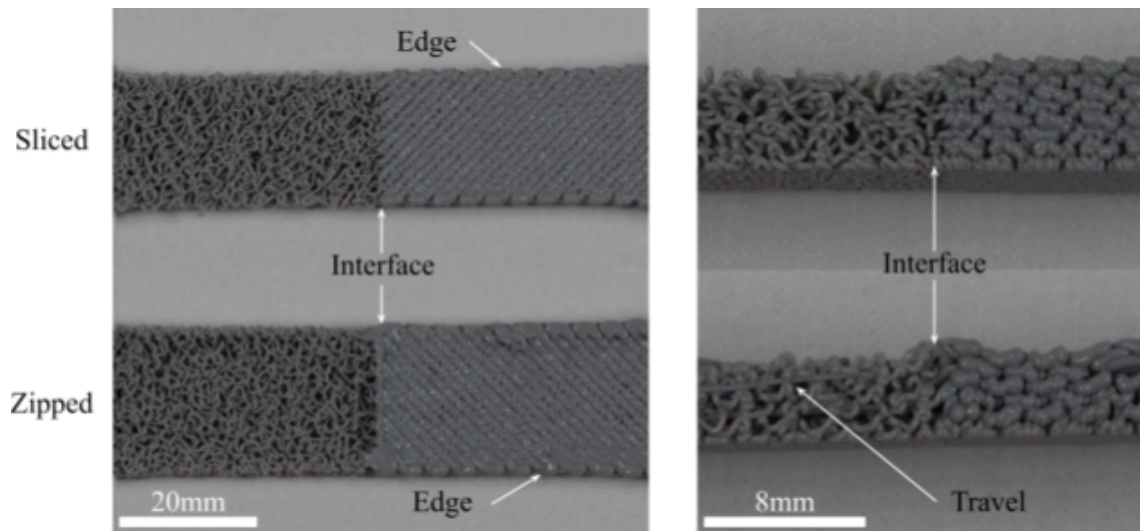


Figure 5. Annotated comparison of printed specimens using this paper’s custom sliced toolpath generation method vs previous “zipped” method from the top and side profiles respectively.

Results

Figure 5 illustrates the impacts of the two slicing methods. The upper row presents the result of our new slicing algorithm creating a continuous toolpath, while the lower row depicts a specimen created using the zipped method. Both cases reveal a distinct interface between $V^* = 0.40$ and $V^* = 0.15$. However, a noticeable 'bump' artifact emerges in the side view of the zipped version, resulting from the overlapping printed paths at the interface. The two slicers have qualitatively different edge crispness, as the zipped method introduces thickening at the edges. Additionally the non continuous movements of the zipped method introduces travel artifacts that are embedded in the print.

This result illustrates the utility of our new slicing method for VTP foams in padding applications such as automotive seats, orthotics, and personal protective equipment. The defects from zipped sections would create unpleasant pressure points in these applications. Our new slicer by contrast produces structures with a less pronounced pressure point.

Figure 4 details the local compressive modulus testing conducted on the dogbone structure. Here, V^* linearly increases from 0.15 to 0.40, with varying transition lengths represented by vertical

black lines for clarity. The compressive modulus remains largely unchanged outside the transition region, whereas inside this region, we observe a distinct modulus alteration. This phenomenon is further investigated in Figure 6 where an exponential curve of the form $f(x) = \lambda e^{\gamma x}$ is fitted solely to the transition regions. In each subplot, the transition region is normalized to length one, allowing for direct comparison of the exponent term, corresponding to the line's slope in the semi-log plot. As the transition region increases (i.e., acquires more data) the γ term converges which indicates that the modulus as a function of V^* is constant for transition lengths greater than zero.

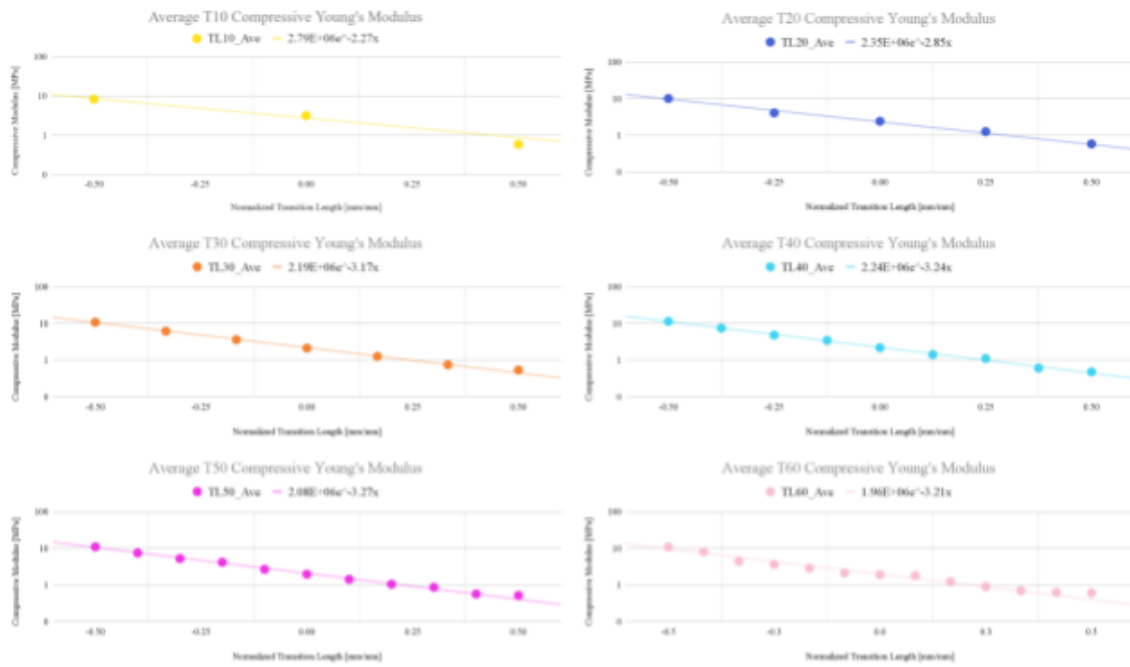


Figure 6. Normalized semi-log plots of average effective compressive Young's Modulus within sample transition zones fitted with exponential trend lines

Figure 7 shows an abbreviated timelapse of the tensile tests from each TL family. The images capture three critical points: test initiation, mid-test at the 35-second mark, and the test conclusion. From these elements we can see that the transition length leads to distributed strain across the top and bottom halves of the samples for transition lengths 20mm and larger. This creates a more uniform transmission between the sections under loading.

Figure 8 presents the mean stress-strain curve for each TL family, enclosed by their respective max and min boundaries. Due to variability in test durations within each TL family, data was truncated at the shortest test time to enable average calculation. The stiffest specimen (V015) is truncated vertically in the topmost plot to focus on the transition specimens, while the most compliant specimen (V040) lies beneath the transition specimens. The stress-strain curves for all TL families closely align, suggesting similar performance in modulus, fracture stress, fracture strain, and toughness. Table 1 and Figure 9 summarize the results from these stress-strain curves.

Discussion

In the discussion of our results, we found that dogbones with transitional regions exhibit similar elasticity to naively zipped dogbones. However, they notably outperform the zipped versions, exhibiting higher fracture stress, enhanced fracture strain, and superior toughness. This improved performance holds even in the context of zero-length transitions (TL00), where the VTP-sliced dogbones outperformed the zipped versions. This is attributed to the continuous toolpath created by our method.

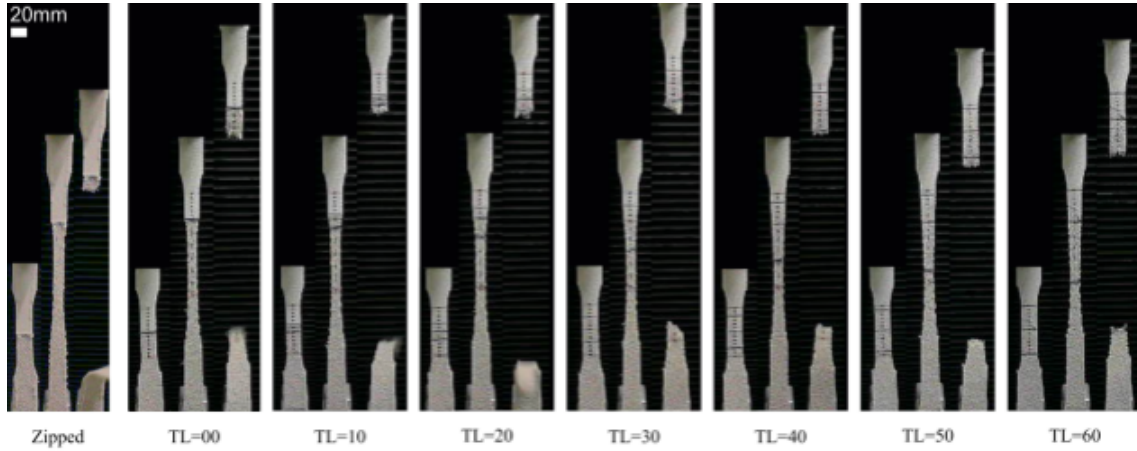


Figure 7. Images taken during testing for each sliced and zipped sample group. Each set from left to right depicts the beginning of testing (no deformation), 35 seconds into testing, and time of failure.

Table 1 shows the tensile modulus averaging 2.046 MPa across all transition families with a standard deviation of 0.115 MPa while the zipped dogbone has a modulus of 2.185 MPa. This indicates that tensile modulus of the dogbones is nominally constant as long as the average value of V^* across the length of the dogbone is constant. We define \bar{V}^* to be the integral of

$$[8] \quad V^*(x, L) = \frac{x}{4L} + \frac{V_{max}^* + V_{min}^*}{2}$$

over the entire length of the dogbone where x is the location on the dogbone and L is the desired transition length. In the case of a linear V^* it is equivalent to the average of the maximum and minimum V^* values multiplied by the dogbone length. This value is constant for both VTP sliced dogbones as well as the zipped dogbones. There is a clear indication that a simple method of determining dogbone tensile equivalence is to compare the \bar{V}^* value obtained from a curve.

While V^* is linear in x , the compressive modulus $E_c(x, L)$ changes exponentially as seen in Figure 4 and Figure 6. We average the values of the exponential fits (γ and λ) from Figure 6 to determine a general fit for the transition region

$$[9] \quad E_c(x, L) = 2.268e^{-3.003\frac{x}{L}}, \quad -\frac{L}{2} \leq x < \frac{L}{2}$$

The modulus is also exponential in V^* because V^* is linear in x . This means that with a logarithmic definition of $V^*(x, L)$ a linear transition of modulus is achievable.

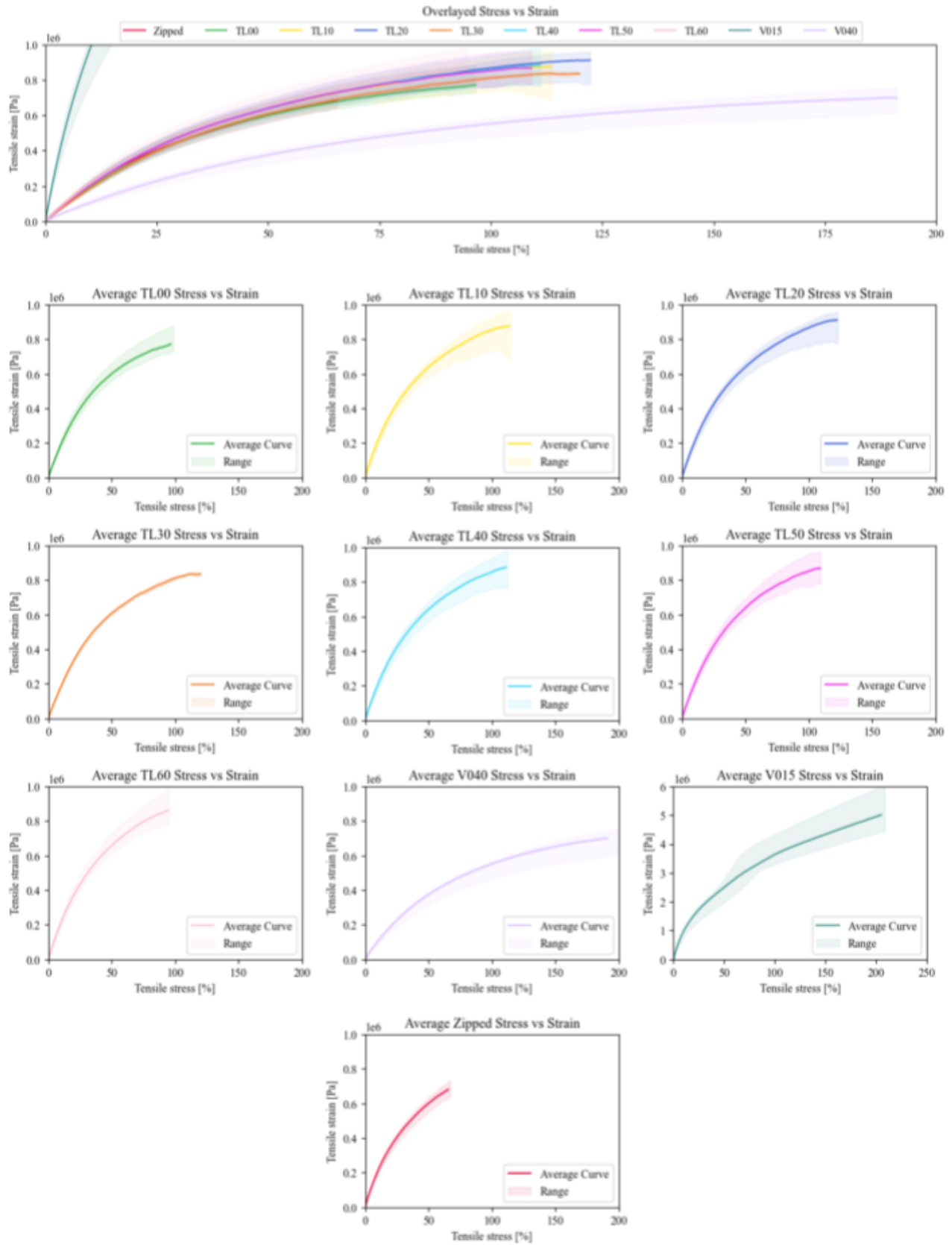


Figure 8. Compiled average stress strain curves for each sample group. Note: each stress-strain curve is truncated to the lowest fracture stress within its given sample group.

Table 1 also shows that the fracture stress, fracture strain, and toughness are consistent regardless of transition length, while the zipped dogbones performed at a much lower level. Predictably, the zipped dogbones, without a continuous toolpath between the differing V^* regions, fractured much earlier than the continuous transitions, likely due print errors and stress concentration at the interface. Compared directly to the TL00 sample, there was an approximate 33% increase in fracture strain and a 10% increase in fracture stress simply by using our continuous toolpath method without any transition length. This demonstrates that simply having a continuous toolpath between disparate areas can significantly improve the reliability of the sample and further benefits are seen when applying the transition over a region.

Table 1. Summary statistics for the tensile tests performed on the dogbones. Each row represents the average followed by standard deviation of 5 tests on dogbones printed with the same parameters. The mean of averages and mean of standard deviations of the samples printed with the new technique are given. The previous state-of-the-art and homogenous dogbone summaries are given at the bottom. No data is presented for V0.40 and V0.15 because the tests did not result in fracture.

Family	Transition Length [mm]	Effective Young's Modulus [MPa]	Fracture Stress [MPa]	Fracture Strain [%]	Toughness [MJ/m ³]
TL00 Average	0	1.944 (0.227)	0.779 (0.090)	120.92 (0.166)	0.717 (0.167)
TL10 Average	10	2.138 (0.237)	0.867 (0.083)	138.55 (0.147)	0.935 (0.164)
TL20 Average	20	2.102 (0.153)	0.888 (0.073)	137.22 (0.111)	0.925 (0.142)
TL30 Average	30	1.843 (0.107)	0.821 (0.021)	134.93 (0.150)	0.840 (0.123)
TL40 Average	40	2.073 (0.185)	0.883 (0.132)	134.52 (0.209)	0.907 (0.265)
TL50 Average	50	2.052 (0.248)	0.851 (0.110)	122.86 (0.142)	0.798 (0.191)
TL60 Average	60	2.169 (0.246)	0.860 (0.098)	120.02 (0.127)	0.782 (0.159)
Mean of Averages	-	2.046 (0.115)	0.850 (0.038)	129.86 (0.082)	0.843 (0.083)
Zipped Average	Zipped	2.185 (0.101)	0.706 (0.074)	87.69 (0.168)	0.457 (0.143)
V0.40 Average	V* 0.40	0.982 (0.069)	-	-	-
V0.15 Average	V* 0.15	12.697 (3.444)	-	-	-

Conclusion

Our study provides evidence of the potential and practicality of fabricating durable, continuously graded mechanical materials using Viscous Thread Printing (VTP). We presented a novel slicing approach that generates seamless toolpaths over several regions, each possessing distinct VTP characteristics. This technique enabled us to create smooth transitions between these regions, serving to minimize stress concentration and enhance the overall reliability of the interface. By applying our method, we observed a 20% increase in fracture stress, a 42% extension in strain before fracture, and an 84% improvement in material toughness compared to conventional methods that don't allow continuous transitions. We further detailed the compressive modulus along the transition, noting its non-linear relationship to V^* , and demonstrated the tensile modulus to be unaffected by transition length.

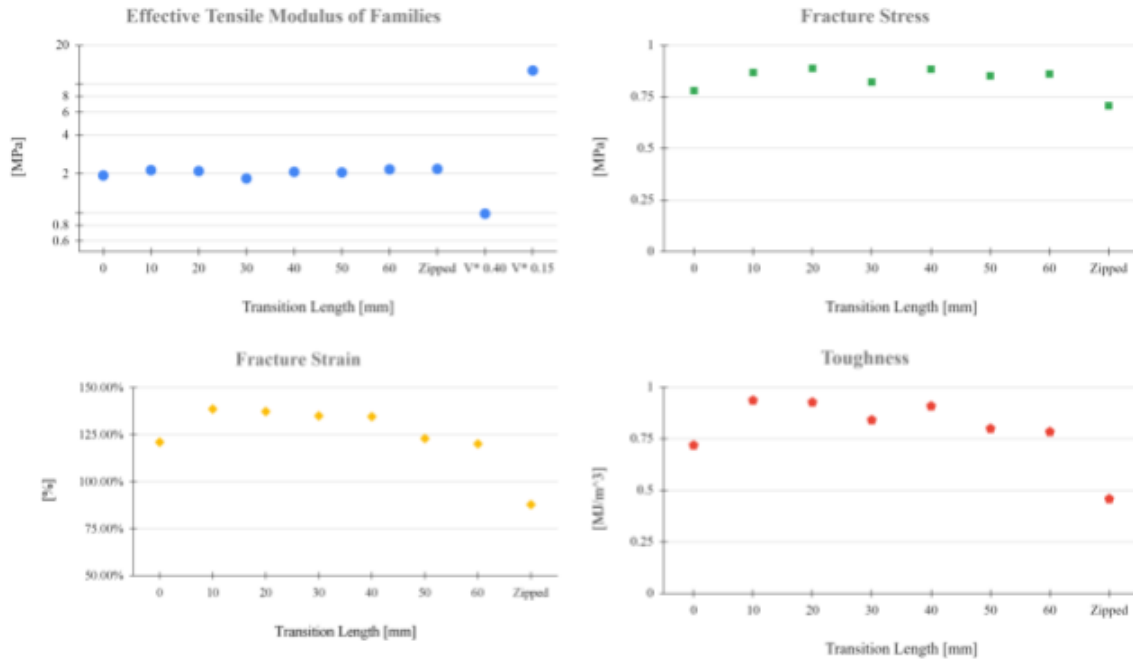


Figure 9. Tensile plots containing significant data from Table 1.

It is clear that arbitrary control of the modulus in the transition region would be beneficial. Currently, we have determined a simple model to predict the compressive modulus as a function of space and transition length. In future studies we intend to apply inverse design and determine the appropriate non-linear mapping of V^* to achieve a desired modulus layout. Additionally, while this work focused on 2.5D structures, we would like to pursue graded material in all three dimensions to fully unlock the possibilities of graded material.

References

1. Lipton JI, Lipson H. 3D Printing Variable Stiffness Foams Using Viscous Thread Instability. *Sci Rep.* 2016;6: 29996. doi:10.1038/srep29996
2. Tappa K, Jammalamadaka U. Novel Biomaterials Used in Medical 3D Printing Techniques. *J Funct Biomater.* 2018;9. doi:10.3390/jfb9010017
3. Lee J-Y, An J, Chua CK. Fundamentals and applications of 3D printing for novel materials. *Applied Materials Today.* 2017;7: 120–133. doi:10.1016/j.apmt.2017.02.004
4. Derby B. Printing and prototyping of tissues and scaffolds. *Science.* 2012;338: 921–926. doi:10.1126/science.1226340
5. Melchels FPW, Domingos MAN, Klein TJ, Malda J, Bartolo PJ, Huttmacher DW. Additive manufacturing of tissues and organs. *Prog Polym Sci.* 2012;37: 1079–1104. doi:10.1016/j.progpolymsci.2011.11.007

6. Chu C, Graf G, Rosen DW. Design for Additive Manufacturing of Cellular Structures. Comput Aided Des Appl. 2008;5: 686–696. doi:10.3722/cadaps.2008.686-696
7. Jin Y, Fang X, Li Y, Torrent D. Engineered Diffraction Gratings for Acoustic Cloaking. Phys Rev Appl. 2019;11: 011004. doi:10.1103/PhysRevApplied.11.011004
8. Li G-H, Wang Y-Z, Wang Y-S. Active control on switchable waveguide of elastic wave metamaterials with the 3D printing technology. Sci Rep. 2019;9: 16226. doi:10.1038/s41598-019-52705-5
9. Fan S-W, Zhao S-D, Cao L, Zhu Y, Chen A-L, Wang Y-F, et al. Reconfigurable curved metasurface for acoustic cloaking and illusion. Phys Rev B Condens Matter. 2020;101: 024104. doi:10.1103/PhysRevB.101.024104
10. Gibson I, Rosen D, Stucker B, Khorasani M. Design for Additive Manufacturing. In: Gibson I, Rosen D, Stucker B, Khorasani M, editors. Additive Manufacturing Technologies. Cham: Springer International Publishing; 2021. pp. 555–607. doi:10.1007/978-3-030-56127-7_19
11. Murr LE, Gaytan SM, Medina F, Martinez E, Martinez JL, Hernandez DH, et al. Characterization of Ti–6Al–4V open cellular foams fabricated by additive manufacturing using electron beam melting. Materials Science and Engineering: A. 2010;527: 1861–1868. doi:10.1016/j.msea.2009.11.015
12. Bauer J, Hengsbach S, Tesari I, Schwaiger R, Kraft O. High-strength cellular ceramic composites with 3D microarchitecture. Proc Natl Acad Sci U S A. 2014;111: 2453–2458. doi:10.1073/pnas.1315147111
13. Nguyen J, Park S-I, Rosen D. Heuristic optimization method for cellular structure design of light weight components. International Journal of Precision Engineering and Manufacturing. 2013;14: 1071–1078. doi:10.1007/s12541-013-0144-5
14. Cheng L, Zhang P, Biyikli E, Bai J, Pilz S, To AC. Integration of topology optimization with efficient design of additive manufactured cellular structures. 2015 International. 2015 [cited 1 Jul 2023]. Available: <https://repositories.lib.utexas.edu/handle/2152/89424>
15. Morris SW, Dawes JHP, Ribe NM, Lister JR. Meandering instability of a viscous thread. Phys Rev E Stat Nonlin Soft Matter Phys. 2008;77: 066218. doi:10.1103/PhysRevE.77.066218
16. Brun P-T, Audoly B, Ribe NM, Eaves TS, Lister JR. Liquid ropes: a geometrical model for thin viscous jet instabilities. Phys Rev Lett. 2015;114: 174501. doi:10.1103/PhysRevLett.114.174501
17. Srivastava S, Driessen T, Jeurissen R, Wijshoff H, Toschi F. LATTICE BOLTZMANN METHOD TO STUDY THE CONTRACTION OF A VISCOUS LIGAMENT. Int J Mod

Phys C. 2013;24: 1340010. doi:10.1142/S012918311340010X

18. Yuk H, Zhao X. A New 3D Printing Strategy by Harnessing Deformation, Instability, and Fracture of Viscoelastic Inks. *Adv Mater.* 2018;30. doi:10.1002/adma.201704028
19. Emery B, Revier D. Applied Viscous Thread Instability for Manufacturing 3D Printed Foams. *Proceedings of the 7th Annual ACM Symposium on Computational Fabrication.* New York, NY, USA: Association for Computing Machinery; 2022. pp. 1–2. doi:10.1145/3559400.3565596
20. Palma M. Grading Threads. Exploiting Viscous Thread Instability for the additive fabrication of Functionally Graded Structures via sensor-adaptive robotic control. *Architecture, Structures and Construction.* 2023;3: 171–191. doi:10.1007/s44150-023-00089-6
21. Slic3r. In: Slic3r [Internet]. [cited 1 Jul 2023]. Available: <https://github.com/slic3r/Slic3r>
22. NinjaTek NinjaFlex TDS. In: NinjeTek [Internet]. [cited 1 Jul 2023]. Available: <https://ninjatek.com/shop/ninjaflex/>
23. Carbon Uma-90 TDS. In: Carbon3D [Internet]. [cited 1 Jul 2023]. Available: <https://www.carbon3d.com/materials/uma-90>